Article | Open Access

Energy Materials

Liu *et al. Energy Mater.* **2026**, *6*, 600086 **DOI:**10.20517/energymater.2024.138

A universal Ti_3C_2 assisted strategy facilitates hole extraction of PEDOT:PSS anode interface layer for over 19% efficiency organic photovoltaics

Yi-lin Liu[1,#], Xiaojian Zheng[1,2,#], Gaoyang Wang[1], Wenquan Wang[1], Jing Guo[3], Luobin She[1], Zhixin Liu[1,2], Zhenye Li[1,*], Xingzhu Wang[1,2,*]

Keywords:
Titanium carbide, organic photovoltaic, anode interface layer, conductivity, hole extraction

Citation: Liu, Y. L.; Zheng, X.; Wang, G.; Wang, W.; Guo, J.; She, L.; Liu, Z.; Li, Z.; Wang, X. A universal Ti_3C_2 assisted strategy facilitates hole extraction of PEDOT:PSS anode interface layer for over 19% efficiency organic photovoltaics. *Energy Mater.* **2026**, *6*, 600086. https://dx.doi.org/10.20517/energymater.2024.138

Received: 26 Aug 2024 **First Decision:** 7 Nov 2024 **Revised:** 19 Jan 2025 **Accepted:** 1 Apr 2025 **Published:** 29 Jul 2026

Academic Editors: Yuping Wu, Wei Tang **Copy Editor:** Ping Zhang **Production Editor:** Ping Zhang

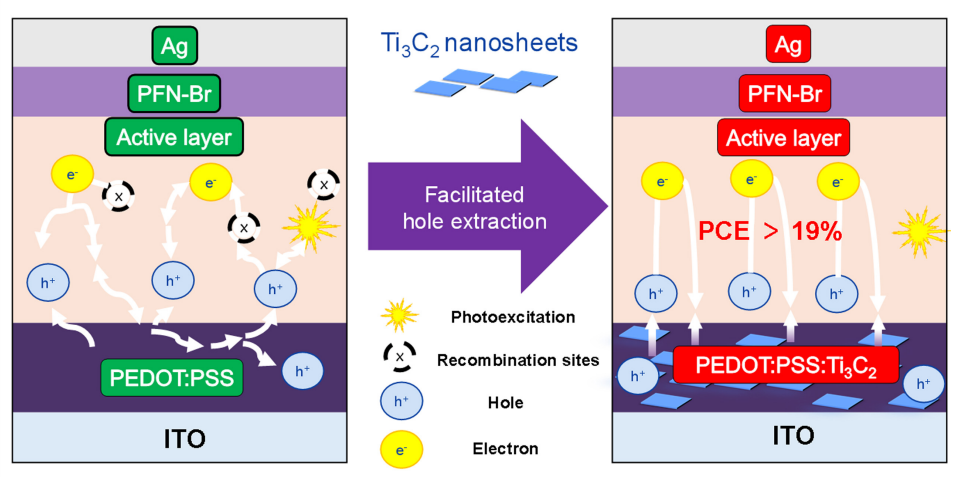

Abstract

Low hole extraction efficiency is a key factor restricting the performance of organic photovoltaics (OPVs). Improving the conductivity of PEDOT:PSS [poly(3,4-ethylenedioxythiophene):poly(styrenesulfonate)] and reducing its large extraction barrier with the active layer is viewed as an important direction to increase the hole extraction efficiency of OPVs. In this work, few-layer two-dimensional titanium carbide (Ti_3C_2) nanosheets were prepared by HCl/LiF etching and doped into PEDOT:PSS to fabricate OPV devices. Ti_3C_2 nanosheets induced the configuration transformation of PEDOT from spiral benzoyl to linear quinone structure, form tightly packed large-size PEDOT nanocites, and connect these conductive nanocites to construct a new charge transport channel, thus boosting the conductivity of the PEDOT:PSS anode interface layer. In addition, Ti_3C_2 nanosheets adjusted the work function of PEDOT:PSS, thus decreasing the hole extraction

[1]College of Mechanical Engineering and School of Electrical Engineering, University of South China, Hengyang 421001, Hunan, China.
[2]Engineering and Research Center for Integrated New Energy Photovoltaics & Energy Storage Systems of Hunan Province, University of South China, Hengyang 421001, Hunan, China.
[3]School of Pharmaceutical Science, University of South China, Hengyang 421001, Hunan, China.
[#]Authors contributed equally.

***Correspondence to:** Prof. Zhenye Li, College of Mechanical Engineering, University of South China, Hengyang 421001, Hunan, China. E-mail: lizhenye@usc.edu.cn; Prof. Xinzhu Wang, Engineering and Research Center for Integrated New Energy Photovoltaics & Energy Storage Systems of Hunan Province and School of Electrical Engineering, University of South China, Hengyang 421001, Hunan, China. E-mail: 2022000041@usc.edu.cn

barrier in OPVs. As 2% volume of Ti_3C_2 doping into PEDOT:PSS interlayer, the maximum power conversion efficiency of PTzBI-oF:PYF-T-o, D18:L8-BO, and PM6:L8-BO-based OPVs boosted from 15.61%, 17.92% and 15.49% to 16.83%, 19.05% and 17.33%, respectively. Our work can provide guidance for facilitating hole extraction of PEDOT:PSS, which is expected to contribute to the further progress of OPVs.

INTRODUCTION

Organic photovoltaics (OPVs) are considered to be a promising low-cost renewable and clean energy because of their light weight, excellent mechanical properties and large-scale production[1-4]. The common device structure of OPVs can be divided into forward devices and reverse devices, where the high efficiency OPVs reported in the literature almost employed forward device structure. Benefitting from the prominent development of donor/acceptor materials, the power conversion efficiency (PCE) of forward OPVs approaches 20%[5,6]. In conventional OPVs, the development of anode interfacial layers (AILs) has progressed substantially slower compared to cathode interfacial layers, primarily due to the limited availability of suitable materials for AIL applications[7-16]. PEDOT:PSS, a conductive polymer blend of poly(3,4-ethylenedioxythiophene) and poly(styrenesulfonate), is widely utilized as an AIL in conventional architecture OPVs, primarily due to its exceptional optical transparency, solution processability, and aqueous solubility[17,18]. Although PEDOT:PSS is in a monopoly position, its own defects are also prominent, which seriously affects its practical application[19-21]. For example, PEDOT:PSS exhibits low conductivity and large extraction barrier with the active layer, which significantly influenced the current mainstream efficient donor with deeper energy level. Therefore, improving the conductivity of PEDOT:PSS and reducing its large extraction barrier with the active layer is viewed as an important strategy to increase the hole extraction efficiency of OPVs[22,23].

The methods of improving the conductivity of PEDOT:PSS can be divided into physical methods and chemical methods[24,25]. Physical methods, such as ultraviolet (UV) light irradiation, improved the conductivity and work function of the PEDOT:PSS film[26]. However, the photovoltaic performance is not significantly improved as the photo-treated or heat-treated PEDOT:PSS films applied to OPVs[27,28]. Chemical methods include adding PEDOT:PSS aqueous solution with an alcohol-soluble polar solvent or slowly fumigating PEDOT:PSS film with solvent steam[29,30], treating the surface of the film with a surfactant[31], and adding PEDOT:PSS aqueous solution with a PH of 1-3 strong acid[32]. However, these modification methods may damage the surface morphology of the thin film or impair the stability of OPVs. In addition to the above modification methods, salt solution doping is most commonly used. Systematic study found that the introduction of Cu^{2+}, Ag^{+}, In^{3+} has a positive effect on device performance, while the introduction of Na^{+}, Li^{+}, Mg^{2+} will destroy device performance[33].

The two-dimensional transition metal carbide Ti_3C_2 exhibits excellent hydrophility, high visible light transmittance and abundant surface functional groups[34,35], which is expected to improve the conductivity of PEDOT:PSS. In this work, few-layer Ti_3C_2 nanosheets were prepared by HCl/LiF etching and doped into PEDOT:PSS to fabricate OPV devices. Ti_3C_2 nanosheets induce the configuration transformation of PEDOT from spiral benzoyl to linear quinone structure, form tightly packed large-size PEDOT nanocites, and connect these conductive nanocites to construct a new charge transport channel, thus boosting the conductivity of the PEDOT:PSS film. Furthermore, the incorporation of Ti_3C_2 as a dopant effectively modulated the work function of PEDOT:PSS, resulting in a significant reduction of the hole extraction barrier at the anode interface in OPV devices. As a result, the maximum PCE of PTzBI-oF:PYF-T-o, D18:L8-BO, and PM6:L8-BO devices boosted from 15.61%, 17.92% and 15.49% to 16.83%, 19.05% and 17.33%, respectively.

EXPERIMENTAL

Materials

The organic materials D18, PM6, PYF-T-o, and L8-BO were sourced from Nanjing Zhiyan Technology Co., Ltd. (China). PTzBI-oF and PFN-Br were procured from Dongguan Fu'an Photoelectric Technology Inc., Ltd. (China). High-purity solvents, including chloroform (CF) and 1-chloronaphthalene (1-CN), along with PEDOT:PSS, were obtained from Sigma-Aldrich (USA).

Fabrication of OPVs

The pre-patterned indium tin oxide (ITO)-coated glass substrates underwent a sequential cleaning process, beginning with detergent washing, followed by ultrasonic treatment in deionized water, acetone, and isopropyl alcohol (20 min for each solvent), and concluding with overnight drying in an oven[36]. The AIL was deposited by spin-coating the precursor solution onto oxygen plasma-treated ITO substrates (5 min treatment) at 3000 rpm for 30 s, followed by thermal annealing at 150 °C for 15 min to achieve optimal film properties[37]. For the PTzBI-oF:PYF-T-o blend system, the donor-acceptor weight ratio was maintained at 1:1.4 (w/w), with PTzBI-oF concentration fixed at 6 mg mL^{-1}. The active layer was fabricated by spin-coating the blend solution in CF (containing 0.5 vol% 1-CN as an additive) at 2000 rpm for 30 s, yielding uniform thin films with a thickness of approximately 120 nm. In the PM6:L8-BO photovoltaic system, the donor:acceptor ratio was optimized at 1:1.2 (w/w), with the PM6 concentration maintained at 5 mg mL^{-1}. The active layer was deposited by spin-coating the blend solution in CF (containing 0.5 vol% 1-CN as processing additive) at 4000 rpm for 30 s, resulting in uniform thin films with a thickness of approximately 100 nm. In the D18:L8-BO photovoltaic system, the donor:acceptor ratio was maintained at 1:1.2 (w/w), with the D18 concentration fixed at 4.3 mg mL^{-1}. The active layer was fabricated by spin-coating the blend solution in CF (containing 0.5 vol% 1-CN as processing additive) at 3500 rpm for 30 s, yielding uniform thin films with a thickness of approximately 100 nm. Subsequently, the films were subjected to thermal annealing at 100 °C for 5 min to optimize their morphological and electronic properties[38]. A methanol solution of PFN-Br (0.5 mg mL^{-1}) was subsequently spin-coated onto the active layer at 2000 rpm for 30 s to form the cathode interfacial layer. Finally, a 100 nm-thick silver electrode was thermally evaporated under high vacuum conditions (< 1×10^{-4} Pa) to complete the device fabrication[39].

Mobility characterization

The hole-only PTzBI-oF:PYF-T-o device with the structure of ITO/(PEDOT:PSS or Ti_3C_2:PEDOT:PSS)/PTzBI-oF:PYF-T-o/MoO_3/Ag was fabricated to determine mobility μ by the formula $J = (9/8)\varepsilon_0\varepsilon_r\mu V_{eff}^2/d^3$, in which J, μ, ε_0, ε_r, d and V_{eff} delegate the current density, zero-field charge mobility at, free-space permittivity, material's relative permittivity, the thickness of PTzBI-oF:PYF-T-o layer and effective voltage, respectively.

Instruments used for characterization

The absorption and photoluminescence (PL) spectra of PTzBI-oF, PYF-T-o, PTzBI-oF:PYF-T-o, PEDOT:PSS and Ti_3C_2:PEDOT:PSS substances were analyzed by utilizing an absorption photoluminescence spectral analysis system (APLS-AS), specifically model APL-AS II. The current density-voltage (J-V) curves of PTzBI-oF:PYF-T-o (1:1.4) devices, both with and without Ti_3C_2 incorporated in the PEDOT:PSS interlayer, were measured using a computer-controlled Keithley 2450 SourceMeter. These measurements were conducted under AM 1.5G irradiation provided by a solar simulator (Sirius-SS150A, 150W AAA grade, manufactured by Zolix Instruments). The external quantum efficiency (EQE) spectra of PTzBI-oF:PYF-T-o (1:1) devices with (or without) Ti_3C_2 in the PEDOT:PSS interlayer were measured with a self-built external quantum measurement system (Zolix Instruments) calibrated with standard silicon cells. Impedance spectrum of PTzBI-oF:PYF-T-o (1:1) devices with (or without) Ti_3C_2 in the PEDOT:PSS interlayer was measured by utilizing an electrochemical workstation (interface 1010). Transient absorption (TA) spectra

were obtained by comparing the probe light spectra with and without pump light excitation (an 805 nm seed light with a single pulse energy was used). The transient photocurrent (TPC) and transient photovoltage (TPV) characteristics of devices were measured by the TPC/photovoltage test system (CEL-TPV2000). Atomic force microscopy (AFM) graphics of PEDOT:PSS and Ti_3C_2:PEDOT:PSS substances were captured by utilizing a Bruker Multimode 8 Microscope. Energy dispersive spectrometer (EDS) images were performed using the Czech TESCAN MIRA LMS scanning electron microscope. The transmission electron microscopy (TEM) images of a few-layer Ti_3C_2 nanosheet were performed using the JEM-F200 instrument from Japan Electronics. X-ray diffraction (XRD) of a few-layer Ti_3C_2 nanosheet was performed by using an X-ray diffuser (Bruker, D8 Advance, λ = 0.15418 nm). Grazing incidence wide-angle X-ray scattering (GIWAXS) of sample films was performed by using an Incidence Wide-Angle X-ray diffuser (Xeuss 2.0, λ = 1.54189 Å). X-ray photoelectron spectroscopy (XPS) analysis of PEDOT:PSS and Ti_3C_2:PEDOT:PSS substances was conducted using the Thermo Fischer Nexsa system. The water and oil contact angle (CA) θ of PTzBI-oF, PYF-T-o, PEDOT:PSS and Ti_3C_2:PEDOT:PSS substances were obtained by a Dataphysics OCA40 Micro surface CA analyzer.

RESULT AND DISCUSSION

Preparation steps and detailed manifestation of few-layer Ti_3C_2 nanosheets

The block Ti_3AlC_2 material was etched with hydrofluoric acid produced *in situ* by hydrochloric acid and lithium fluoride [Figure 1A]. The specific experimental process was as follows: 20 mL 9 mol/L hydrochloric acid was put into a polytetrafluoroethylene beaker, slowly added 1.6 g LiF, and stirred for 5 min. 1 g of 400 mesh Ti_3AlC_2 powder was slowly added to the above mixture and continuously stirred at 36 °C for 24 h. After the etching, 5 mL of liquid was added to 30 mL of deionized water, centrifuged at 3500 r/min for 5 min, and the cleaning was finished when the pH value of the supernatant was 6 to 7. The precipitated substance obtained after centrifugation is freeze-dried, and the powder obtained after freeze-drying is multilayer Ti_3C_2. 500 mg of multilayer Ti_3C_2 was put into 30 mL of deionized water, protected by Ar gas, and sonicated in an ice water bath for 30 min. After sonication, the solution was centrifuged at 3500 r/min for 1 h, and the supernatant was taken as few-layer Ti_3C_2 nanosheets.

A TEM image for a few-layer Ti_3C_2 nanosheet solution is shown in Figure 1B and C, where its surface is relatively flat and smooth, its edge is clear and dry, and there are no obvious holes on the sheet, which proves that this nanosheet obtained by this method has less defects. From the XRD pattern of Ti_3C_2 films [Figure 1D], not only the obvious (002) characteristic peak at 5.9° was observed, but also the (004), (006), (008), (010) and (012) crystal faces were observed in the range of $5° \leq 2\theta \leq 60°$, demonstrating that Ti_3C_2 has been successfully etched and the layers are well separated, forming highly ordered crystal structure.

Effect of Ti_3C_2 nanosheets on the photoelectric properties of PEDOT:PSS

Ti_3C_2 nanosheets have good electrical conductivity and water solubility, and the addition of Ti_3C_2 nanosheets to PEDOT:PSS can form a uniform solution without precipitation. Supplementary Figure 1 displays the preparation process of the Ti_3C_2:PEDOT:PSS interlayer. The device structure of OPVs with Ti_3C_2:PEDOT:PSS hybrid AIL was shown in Figure 2A, and the chemical structures for PEDOT:PSS, Ti_3C_2, PTzBI-oF, PYF-T-o and PFN-Br were displayed in Figure 2B and C, Supplementary Figure 2, respectively. As shown in XPS of Ti_3C_2:PEDOT:PSS hybrid AIL [Figure 2D], the characteristic S 2p peak around 168 eV corresponded to S element in PEDOT:PSS, and O 1s peak located at about 531 eV was attributed to the O element in PEDOT:PSS. The Ti 2p peak located at about 453 eV in the XPS of Ti_3C_2:PEDOT:PSS hybrid AIL, certificating the few-layer Ti_3C_2 was successfully embedded into the PEDOT:PSS component. As shown in the EDS images [Supplementary Figure 3], Ti element was evenly distributed in PEDOT:PSS interlayer, further indicating that Ti_3C_2 nanosheets exhibit good dispersibility in the PEDOT:PSS interlayer.

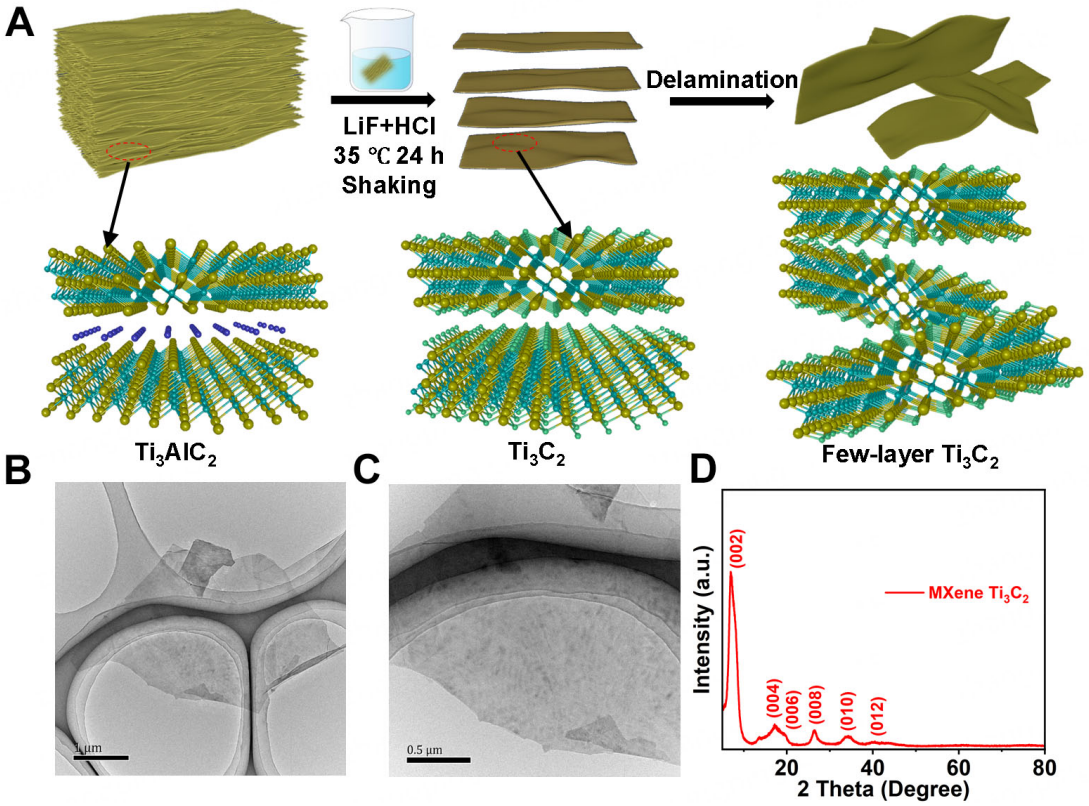

Figure 1. (A) Schematic of the synthesis of few-layer Ti_3C_2 nanosheet; (B and C) The TEM images for few-layer Ti_3C_2 nanosheet with different magnifications; (D) The XRD patterns of few-layer Ti_3C_2 nanosheet. TEM: Transmission electron microscopy; XRD: X-ray diffraction.

Figure 2E illustrates the transmittance variation of PEDOT:PSS films when Ti_3C_2 is incorporated. The luminance of the PEDOT:PSS film increased by 2% in the wavelength range of 300-1000 nm. This enhancement may facilitate the light absorption capacity of the active layer, thereby boosting the photocurrent in OPVs. To confirm our hypothesis, we systematically analyzed the absorption spectra of PTzBI-oF, PYF-T-o, and PTzBI-oF:PYF-T-o membranes that were spin-coated onto PEDOT:PSS films, both with and without the incorporation of Ti_3C_2 nanosheets [Supplementary Figure 4]. As Ti_3C_2 nanosheets added into the PEDOT:PSS interlayer, PTzBI-oF and PYF-T-o films exhibited intensive absorption bands in the range of 450-700 nm and 700-900 nm [Supplementary Figure 4A], respectively. Such strengthened absorption in neat PTzBI-oF (or PYF-T-o) membranes was well retained in PTzBI-oF:PYF-T-o blends [Supplementary Figure 4B], facilitating the photons acquisition in PTzBI-oF:PYF-T-o active layer. Supplementary Figure 5 exhibited the ultraviolet photoelectron spectroscopy (UPS) curves of PEDOT:PSS and Ti_3C_2:PEDOT:PSS interlayer. Interestingly, the measured work function of PEDOT:PSS interlayer increased from 5.00 eV to 5.09 eV with the addition of 2% Ti_3C_2 nanosheet [Supplementary Table 1], which may be related to the charge redistribution caused by Ti_3C_2 dopant induced structural and aggregate state transitions of PEDOT molecules. The energy level variation in PEDOT:PSS induced by Ti_3C_2 mixing and the energy level structure diagram of each functional layer of OPV devices are shown in Figure 2F. The energy level structure of AIL has an important influence on the efficiency of hole extraction, and the more matched the energy level structure, the higher the extraction efficiency[40]. As 2% Ti_3C_2 nanosheet introduced into PEDOT:PSS, its work function (-5.09 eV) is more matched with the highest occupied molecular orbital (HOMO) energy level of PTzBI-oF (-5.25 eV), which is conducive to improving hole extraction efficiency of the device. Therefore, we believe that the OPVs constructed with a more matched hole extraction layer are expected to improve hole extraction efficiency and inhibit the electron-hole recombination, so as to improve

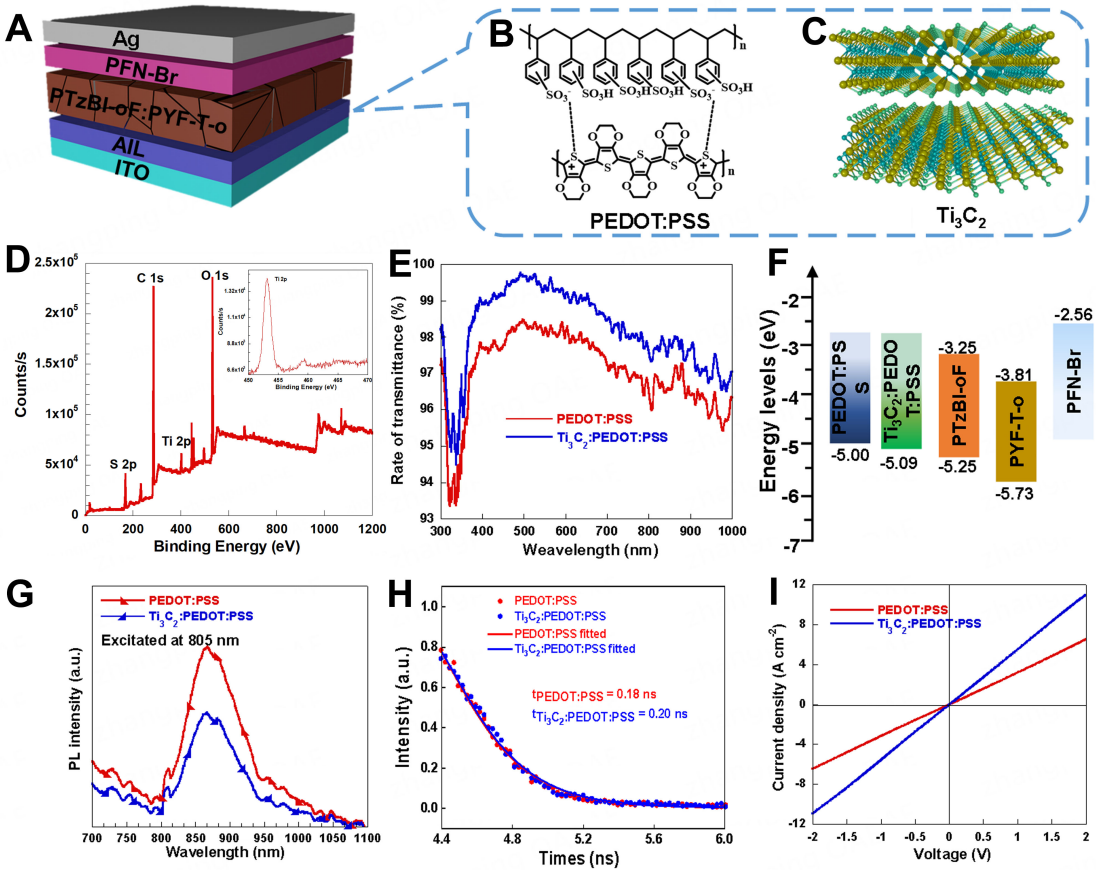

Figure 2. (A) Device structure of OPVs with Ti_3C_2:PEDOT:PSS hybrid AIL; (B) Chemical structures of PEDOT:PSS; (C) Schematic of Ti_3C_2 nanosheet; (D) XPS spectrum of Ti_3C_2:PEDOT:PSS hybrid AIL; (E) Transmittance of hybrid AIL with and without Ti_3C_2 at different wavelengths; (F) The energy level structures of PEDOT:PSS, Ti_3C_2:PEDOT:PSS, PTzBI-oF, PYF-T-o and PFN-Br; (G) PL and (H) TRPL spectrum of PTzBI-oF:PYF-T-o blend films with (or without) Ti_3C_2 in the PEDOT:PSS interlayer; (I) SCLC hole mobility for PTzBI-oF:PYF-T-o devices with (or without) Ti_3C_2 in the PEDOT:PSS interlayer. OPVs: Organic photovoltaics; PEDOT:PSS: poly(3,4-ethylenedioxythiophene):poly(styrenesulfonate); AILs: anode interfacial layers; PL: photoluminescence; TRPL: time-resolved photoluminescence.

the overall performance of the device.

PL spectroscopy was employed to investigate the influence of Ti_3C_2 nanosheets on charge transfer dynamics in OPV devices. The PL spectra of PTzBI-oF:PYF-T-o films deposited on both pristine PEDOT:PSS and Ti_3C_2-doped PEDOT:PSS AIL were systematically analyzed [Figure 2G and Supplementary Figure 6]. Notably, the PTzBI-oF:PYF-T-o layer spin-coated on the Ti_3C_2:PEDOT:PSS AIL exhibited significantly enhanced PL quenching efficiency for both PTzBI-oF and PYF-T-o components, indicating improved charge transfer characteristics that facilitate more efficient hole and electron extraction in the corresponding OPVs[41,42]. The Time-resolved photoluminescence (TRPL) measurements of Ti_3C_2:PEDOT:PSS/PTzBI-oF:PYF-T-o bilayer display a longer decay time of 0.21 ns compared to 0.18 ns for PEDOT:PSS/PTzBI-oF:PYF-T-o bilayer, further confirming efficient hole transfer from active layer to Ti_3C_2:PEDOT:PSS interlayer [Figure 2H]. Electrical conductivity represents a crucial parameter for assessing the performance of interfacial layers. The conductivity measurements of both pristine PEDOT:PSS and Ti_3C_2-incorporated PEDOT:PSS interlayers were conducted using a two-point probe configuration with an ITO/AIL/Ag device structure[43]. The current (I)-voltage (V) characteristics between Ag and ITO strips were measured [Figure 2I]. The electrical conductivity of AIL is derived from Pouillet's law as follows: $V = Id/(\sigma lh)$, where V is the voltage, I is the current passing through AIL film, d is the distance between two ITO

strips, l is the length of ITO strip, h is the thickness of AIL film, and σ is the transverse conductivity of the AIL film[44]. The electrical conductivity measurements revealed significant enhancement upon Ti_3C_2 incorporation, with values of 3.20 × 10^{-3} S m^{-1} for pristine PEDOT:PSS and 5.47 × 10^{-3} S m^{-1} for Ti_3C_2-modified PEDOT:PSS interlayers, respectively [Supplementary Table 2]. To further confirm Ti_3C_2 nanosheets induced the increased conductivity of PEDOT:PSS interlayer, we used the space charge limited current model (SCLC) to calculate the hole mobility (μ_h) of hole-only devices (ITO/AIL/PTzBI-oF:PYF-T-o/MoO_3/Ag) with and without Ti_3C_2 nanosheets in the PEDOT:PSS interlayer [Supplementary Figure 7]. Compared with PTzBI-oF:PYF-T-o devices employing PEDOT:PSS interlayer (1.43 × 10^{-3} cm^2 V^{-1} s^{-1}), PTzBI-oF:PYF-T-o devices employing Ti_3C_2:PEDOT:PSS interlayer displayed dramatically increased μ_h values of 1.58 × 10^{-3} cm^2 V^{-1} s^{-1}, further confirming Ti_3C_2 nanosheets induced the increased conductivity of PEDOT:PSS interlayer that can facilitate fast hole extraction from PTzBI-oF to Ti_3C_2:PEDOT:PSS interlayer [Supplementary Table 3].

Role of Ti_3C_2 doping PEDOT:PSS on the photovoltaic performance of OPVs

To investigate the influence of Ti_3C_2 incorporation on photovoltaic performance, we fabricated OPV devices employing Ti_3C_2-doped PEDOT:PSS as the AIL in a conventional device architecture: ITO/AIL/PTzBI-oF:PYF-T-o/PFN-Br/Ag. The photovoltaic performance for PTzBI-oF:PYF-T-o devices with different Ti_3C_2 doping ratios are shown in Supplementary Figure 8 and Supplementary Table 4, from which it can be seen that 2% volume ratio has the optimal doping effect. Figure 3A and Table 1 show the *J-V* characteristic curve and corresponding photovoltaic performance of PTzBI-oF:PYF-T-o devices with (or without) optimal (2% volume ratio) Ti_3C_2 in PEDOT:PSS interlayer, respectively. The results of device optimization show that Ti_3C_2 doping PEDOT:PSS can significantly improve the performance in PTzBI-oF:PYF-T-o devices, and these improvements are due to the improvement of short-circuit current density (J_{SC}) and fill factor (FF). It was found that the PTzBI-oF:PYF-T-o devices based on Ti_3C_2 doped PEDOT:PSS showed an optimal PCE of 16.83%, which was higher than that of devices based on PEDOT:PSS (15.61%). Among them, J_{SC} and FF of Ti_3C_2-doped PEDOT:PSS devices can reach 25.48±0.49 mA cm^{-2} and 76.23±0.82%, respectively. Notably, PTzBI-oF:PYF-T-o devices based on Ti_3C_2 doped PEDOT:PSS exhibited a smaller series resistance (R_S = 10.27 Ω cm^{-2}) and larger parallel resistance (R_p = 8,745.09 Ω cm^{-2}) than those of devices based on PEDOT:PSS (R_S = 10.46 Ω cm^{-2}, R_p = 4,410.98 Ω cm^{-2}), indicating Ti_3C_2 nanosheets promote the Ohmic contact between the PEDOT:PSS and PTzBI-oF:PYF-T-o layer, thereby boosting the FF of the device. EQE spectra for PTzBI-oF:PYF-T-o devices with (or without) Ti_3C_2 in the PEDOT:PSS interlayer were illustrated in Figure 3B. The PTzBI-oF:PYF-T-o devices based on Ti_3C_2-doped PEDOT:PSS demonstrated a distinctly improved EQE response in the range of 340-850 nm than that of PTzBI-oF:PYF-T-o devices based on PEDOT:PSS, mainly derived from the transmittance enhancement of Ti_3C_2:PEDOT:PSS interlayer. The J_{SC} values obtained from *J-V* curves were well consistent with those ($J_{SC, EQE}$) integrated from EQE spectrum (with a deviation less than 3%). After 160 h of thermal aging at 60 °C [Figure 3C], PTzBI-oF:PYF-T-o devices using Ti_3C_2:PEDOT:PSS as interlayer retained a PCE of 5.1%, while PTzBI-oF:PYF-T-o devices using PEDOT:PSS as interlayer only retained a PCE of 4.1%, implying the Ti_3C_2 nanosheets can improve the thermal stability of PTzBI-oF:PYF-T-o devices.

Doping physical mechanism in PEDOT:PSS for OPVs

The exciton dissociation and charge collection efficiency of the device were studied by plotting the relationship between photocurrent (J_{ph}) and effective applied voltage (V_{eff}) (J_{ph}-V_{eff}). The devices were characterized under different conditions, and the results are shown in Figure 3D. The dissociation efficiency of excitons can be characterized by normalized optical flux density ($\eta_{diss} = J_{ph}/J_{sat}$) when OPVs are in the short-circuit state. At low V_{eff} (< 2V), the J_{ph} of all OPVs reaches saturation[45,46]. Quantitative analysis of exciton dissociation efficiency revealed η_{diss} values of 0.980 and 0.985 for OPVs utilizing pristine PEDOT:PSS and TiO_2-doped PEDOT:PSS interlayers, respectively. The maximum exciton generation rate was calculated

through the relationship $G_{max} = J_{sat}/(qL)$, where q is the elementary charge constant (1.602×10^{-19} C) and L represents the measured thickness of the PTzBI-oF:PYF-T-o photoactive layer[47]. Compared to the reference OPVs with pristine PEDOT:PSS as the AIL, PTzBI-oF:PYF-T-o-based OPVs incorporating Ti_3C_2-doped PEDOT:PSS exhibited significantly enhanced G_{max} [Supplementary Table 5]. This improvement suggests that Ti_3C_2 modification of the PEDOT:PSS interlayer effectively promotes exciton dissociation in the PTzBI-oF:PYF-T-o active layer, consequently leading to enhanced J_{SC} and FF in the photovoltaic devices.

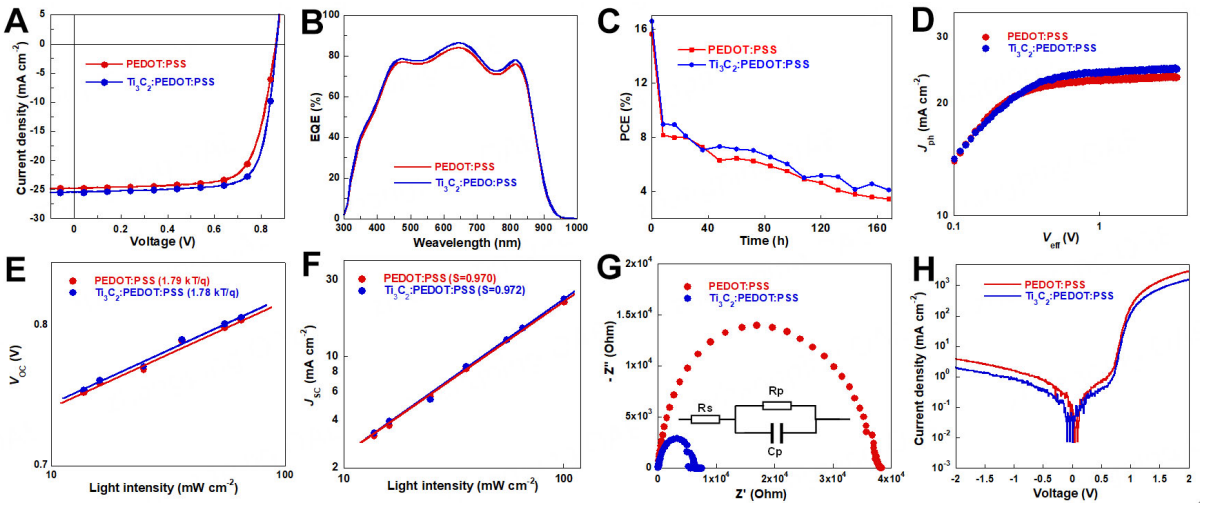

Figure 3. (A) *J-V* characteristic curve, (B) EQE spectrum, (C) thermal stability curve, (D) J_{ph}-V_{eff} curves, V_{OC} (E) and J_{SC} (F) versus P_{light} characteristics, (G) impedance plots, and (H) dark *J-V* curves for PTzBI-oF:PYF-T-o devices with (or without) Ti_3C_2 doping into PEDOT:PSS AIL. *J-V*: Current density-voltage; EQE: external quantum efficiency; J_{ph}: photocurrent; V_{eff}: effective applied voltage; V_{OC}: open-circuit voltage; P_{light}: light intensity; PEDOT:PSS: poly(3,4-ethylenedioxythiophene):poly(styrenesulfonate).

Table 1. Photovoltaic performance for PTzBI-oF:PYF-T-o (1:1.4) devices with (or without) Ti_3C_2 doping into PEDOT:PSS AIL

AIL	V_{OC} (V)	J_{SC} [a] (mA cm^{-2})	$J_{SC, EQE}$ [b] (mA cm^{-2})	FF (%)	PCE $_{avg}$ [c] (%)	PCE $_{max}$ (%)	R_S (Ω)	R_p (Ω)
PEDOT:PSS	0.86±0.01	24.86±0.38	24.39	72.41±0.69	15.35±0.26	15.61	10.46	4410.98
Ti_3C_2:PEDOT:PSS	0.86±0.01	25.48±0.49	25.02	76.23±0.82	16.51±0.32	16.83	10.27	8745.09

[a]Acquired from the corresponding *J-V* curve; [b] Acquired from EQE curves; [c] These values were averaged from 18 independent OPVs; V_{OC}: open-circuit voltage; J_{SC}: short-circuit current density; AILs: anode interfacial layers; FF: fill factor; PCE: power conversion efficiency; PEDOT:PSS: poly(3,4-ethylenedioxythiophene):poly(styrenesulfonate).

To gain a deeper understanding of the reasons for the improved photovoltaic performance, carrier recombination dynamics in these devices can be explored by measuring the functional relationship between open-circuit voltage (V_{OC}), J_{SC} and light intensity (P_{light}). The relationship between the P_{light} and V_{OC} can be expressed as: $V_{OC} \propto nkT/[q\ln(P_{light})]$, where k is the Boltzmann constant, T is the absolute temperature, and q is the fundamental charge[48]. By measuring the V_{OC} of the device under different light intensities, the results shown in Figure 3E were obtained through linear fitting. Analysis of the slops revealed comparable values of n = 1.79 and n = 1.78 for PTzBI-oF:PYF-T-o photovoltaic devices fabricated with conventional PEDOT:PSS and Ti_3C_2-doped PEDOT:PSS interlayers, respectively, suggesting similar recombination characteristics in both device configurations. The light intensity dependence of J_{SC} conforms to the power law relationship: $J_{SC} \propto (P_{light})^S$, where the S value is an exponential factor, and the closer the value is to 1, the charge recombination mechanism of the device tends to be bimolecular recombination mechanism[49]. By measuring the J_{SC} of PTzBI-oF:PYF-T-o device under different light intensities, the results shown in Figure 3F were obtained through linear fitting. Analysis of the recombination parameter (S) revealed values of 0.970 and

0.972 for PTzBI-oF:PYF-T-o photovoltaic devices fabricated with pristine PEDOT:PSS and Ti_3C_2-incorporated PEDOT:PSS interlayers, respectively. The proximity of these S-values to unity strongly indicates that bimolecular recombination is the dominant loss mechanism in both device architectures, while trap-assisted recombination processes are effectively suppressed. Among them, the *S* value of Ti_3C_2:PEDOT:PSS-based devices is closer to 1 compared with PEDOT:PSS-based devices, which helps to enhance J_{SC}.

In order to describe the effect of Ti_3C_2 dopant on the charge transport characteristics of the device, R_S at the interface of the device was measured by impedance spectrum. The electrochemical impedance characteristics of PTzBI-oF:PYF-T-o photovoltaic devices fabricated with PEDOT:PSS and Ti_3C_2-doped PEDOT:PSS interlayers are presented in the Nyquist plots shown in Figure 3G. The experimental data were fitted using an equivalent circuit model to quantitatively determine the charge transport and recombination parameters in both device configurations. A smaller R_S value indicates that Ti_3C_2:PEDOT:PSS has a smaller interface resistance than PEDOT:PSS, which means that the double-anode interface layer has fewer interface trap locations that can effectively reduce the trap-assisted recombination at the interface, resulting in a reduction of non-radiative energy loss[50,51]. The dark current behavior of PTzBI-oF:PYF-T-o photovoltaic devices, fabricated with conventional PEDOT:PSS and Ti_3C_2-incorporated PEDOT:PSS AIL, is presented in the dark *J-V* characteristics shown in Figure 3H. The leakage current density in PTzBI-oF:PYF-T-o device employing Ti_3C_2:PEDOT:PSS as AIL slightly decreased compared with that of PTzBI-oF:PYF-T-o device employing PEDOT:PSS as AIL, indicating that Ti_3C_2 dopant promoted the ohmic contact between the PEDOT:PSS and PTzBI-oF:PYF-T-o layer, and thus boosting the hole extraction of the device.

TPV and TPC were used to probe electron extraction and recombination dynamics [Figure 4A and B][52,53]. Fitting TPV signal by utilizing the formula $y = Aexp(-x/\tau)$, PTzBI-oF:PYF-T-o devices employing Ti_3C_2:PEDOT:PSS as AIL deliver a longer decay time (τ = 0.61 μs) than that of PTzBI-oF:PYF-T-o devices using PEDOT:PSS as AIL (τ = 0.51 μs), providing a longer carrier lifetime for hole extraction and then collected by cathode. The hole extraction time from TPC was estimated to be 1.45 μs and 1.37 μs for PTzBI-oF:PYF-T-o devices using PEDOT:PSS and Ti_3C_2:PEDOT:PSS interlayers, respectively, indicative of the accelerated hole extraction property of PEDOT:PSS interlayer after inserting Ti_3C_2 nanosheets. TA spectra of PEDOT:PSS/PTzBI-oF:PYF-T-o and Ti_3C_2:PEDOT:PSS/PTzBI-oF:PYF-T-o bilayers were measured to study the hole transfer kinetics at the PEDOT:PSS/PTzBI-oF:PYF-T-o interface. As shown in the two-dimensional color diagram [Figure 4C and D], TA spectra [Figure 4E and F] and trace kinetic of ground state bleaching (GSB) signals [Figure 4G and H] of PEDOT:PSS/PTzBI-oF:PYF-T-o and Ti_3C_2:PEDOT:PSS/PTzBI-oF:PYF-T-o bilayers, the observed bleaching peak at 600-690 nm and 790-850 nm represented GSB for PTzBI-oF and PYF-T-o, respectively. The GSB signal of Ti_3C_2:PEDOT:PSS/PTzBI-oF:PYF-T-o bilayer decayed rapidly, indicating that the incorporation of Ti_3C_2 nanosheets into PEDOT:PSS interlayer can enhance the hole transfer at PEDOT:PSS/PTzBI-oF:PYF-T-o interface.

Mechanism analysis for increased mobility of Ti_3C_2 doping PEDOT:PSS interlayer

The surface morphology of PEDOT:PSS interlayer with (or without) Ti_3C_2 was measured by AFM. As shown in Figure 5A and B, the height image of PEDOT:PSS clearly shows many crystal particles clustered together and fine particles are distributed on the polymer chain as Ti_3C_2 doped into PEDOT:PSS. The PEDOT:PSS grains and the PEDOT enrichment domain increase significantly after Ti_3C_2 doping, which also contributes to the improvement of the conductivity after Ti_3C_2 doping. The roughness of PEDOT:PSS is 1.59 nm, which is reduced to 1.47 nm with Ti_3C_2 adulterating into PEDOT:PSS interlayer, mainly due to the enrichment PEDOT on PEDOT:PSS surface. The reduced surface roughness facilitates improved interfacial contact formation with the subsequent active layer while effectively preventing the diffusion of active layer materials into the PEDOT:PSS matrix. This optimized interface morphology contributes to the enhanced J_{SC} and FF

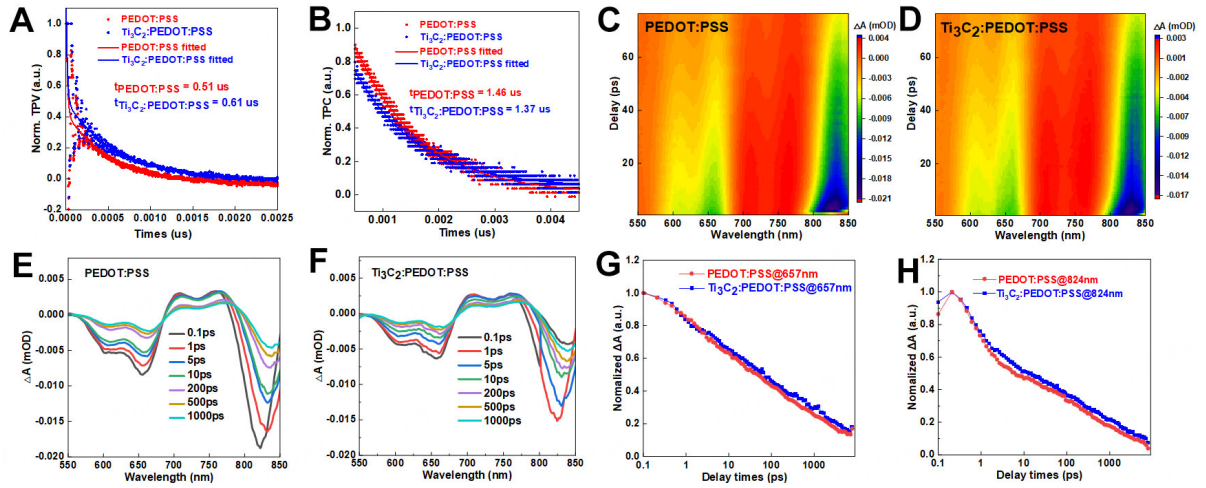

Figure 4. (A) TPV and (B) TPC for PTzBI-oF:PYF-T-o devices with and without Ti_3C_2 doping in the PEDOT:PSS interlayer; (C and D) Two-dimensional TA color plots, (E and F) TA spectra and (G and H) the trace kinetic of GSB signals of PEDOT:PSS/PTzBI-oF:PYF-T-o and Ti_3C_2:PEDOT:PSS/ PTzBI-oF:PYF-T-o bilayers. TPV: Transient photovoltage; TPC: transient photocurrent; PEDOT:PSS: poly(3,4-ethylenedioxythiophene):poly(styrenesulfonate); TA: transient absorption; GSB: ground state bleaching.

observed in the photovoltaic devices. As shown in Figure 5C and D, the phase image of PEDOT:PSS clearly shows PEDOT was slightly separated from PSS as Ti_3C_2 doped into PEDOT:PSS, which may be a key factor in the increased mobility[54]. The phase separation of PEDOT and PSS often results in changes in the surface composition of PEDOT:PSS films. Therefore, the degree of phase separation between PEDOT and PSS can be determined by the analysis of the surface composition of PEDOT:PSS films.

The effect of Ti_3C_2 nanosheets on the crystalline packing of PEDOT:PSS was studied using GIWAXS, with the scattering images and averaged I-q curves in the out-of-plane (OOP) directions displayed in Figure 5E-G. The significantly pronounced π-π stacking reflections in the OOP direction for Ti_3C_2:PEDOT:PSS films indicate that Ti_3C_2 nanosheets induce a preferential face-on orientation of PEDOT:PSS interlayer [Supplementary Table 6], which improve the conductivity and facilitate fast hole transport capacity in the PEDOT:PSS interlayer.

Surface wettability characteristics of PTzBI-oF, PYF-T-o, PEDOT:PSS, and Ti_3C_2-doped PEDOT:PSS films were evaluated through CA measurements using both water and ethylene glycol as probe liquids [Figure 5H]. These measurements provide critical insights into the interfacial compatibility between the donor/acceptor materials (PTzBI-oF/PYF-T-o) and the respective AIL (PEDOT:PSS/Ti_3C_2:PEDOT:PSS)[55]. Surface energy (γ) calculations were performed based on the modified Young's equation $(1 + \cos\theta)\gamma_{p1} = 2(\gamma_s^d \gamma_{p1}^{d\,1/2}) + 2(\gamma_s^p \gamma_{p1}^{p\,1/2})$, where θ is the measured CA, γ_s and γ_{p1} correspond to the total surface energies of the solid sample and testing liquid, respectively[56]. Quantitative analysis of solubility parameters was performed according to the equation $\delta = K\gamma_s^{1/2}$, where δ represents the solubility parameter, K is the proportionality constant (116×10^3 $m^{-1/2}$)[57,58]. This calculation was applied to characterize the solubility properties of PTzBI-oF, PYF-T-o, pristine PEDOT:PSS, and Ti_3C_2-incorporated PEDOT:PSS materials. Detailed CA, δ, and γ parameters of PTzBI-oF, PYF-T-o, PEDOT:PSS, and Ti_3C_2:PEDOT:PSS were listed in Table 2. The Flory-Huggins interaction parameter (χ) that determined by the formula $\chi_{ab} = V_0(\delta_a\text{-}\delta_b)^2/RT$, (where χ_{ab}, V_0, R, and T represent the interaction parameters between a and b, average molar volumes, gas constant, and Kelvin temperature, respectively)[59], can be used to describe the interaction between a and b. The mutual force between PTzBI-oF (or PYF-T-o) and PEDOT:PSS significantly changed as Ti_3C_2 doping into PEDOT:PSS interlayer, proving

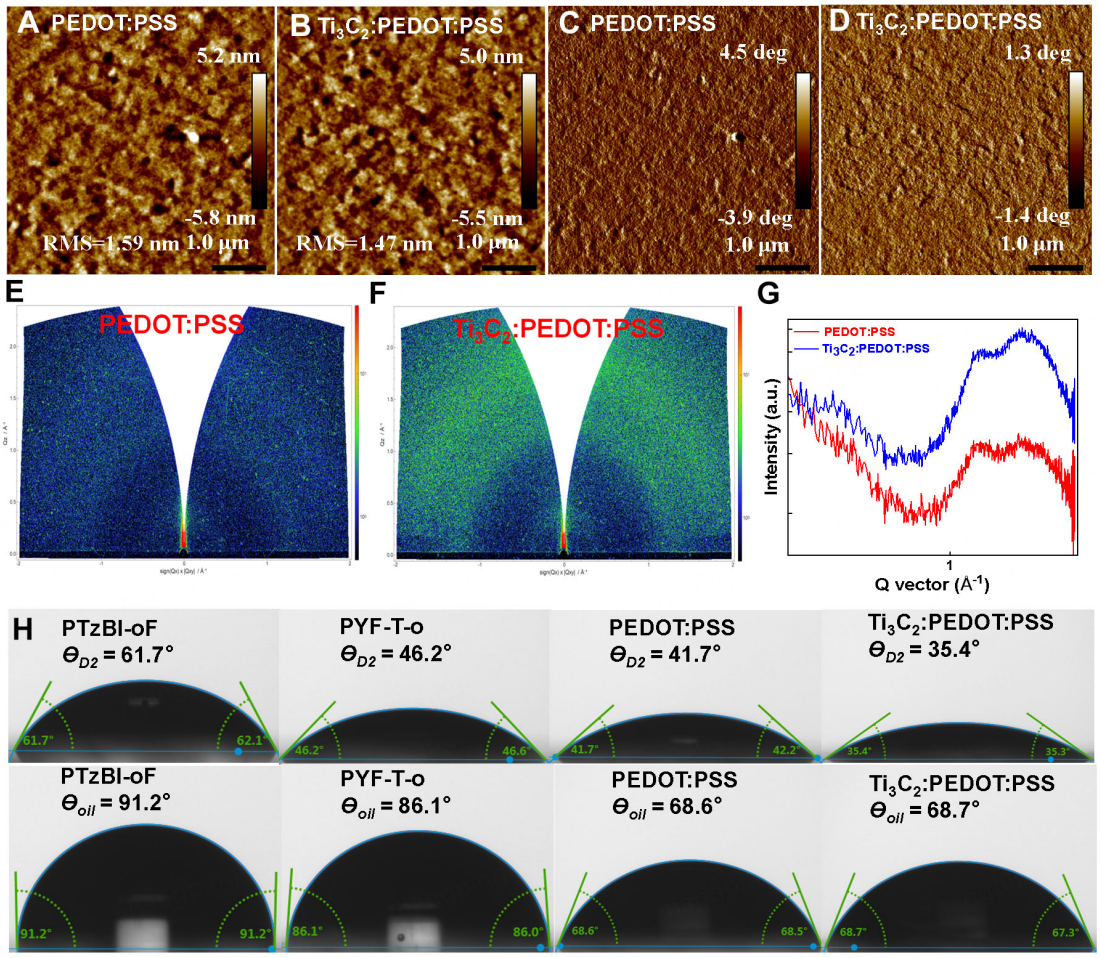

Figure 5. (A and B) AFM height images and (C and D) phase graphics of pristine PEDOT:PSS and Ti_3C_2-incorporated PEDOT:PSS films; GIWAXS profiles of (E) pristine PEDOT:PSS and (F) Ti_3C_2-incorporated PEDOT:PSS films; (G) one-dimensional integrated scattering profiles for PEDOT:PSS with or without Ti_3C_2; (H) Views of surface contact angle measurements for PTzBI-oF, PYF-T-o, pristine PEDOT:PSS, and Ti_3C_2-incorporated PEDOT:PSS films. AFM: Atomic force microscopy; PEDOT:PSS: poly(3,4-ethylenedioxythiophene):poly(styrenesulfonate); GIWAXS: grazing incidence wide-angle X-ray scattering.

Table 2. Surface properties (contact angle, solubility parameter, surface energy, Flory-Huggins parameters) of PTzBI-oF, PYF-T-o, pristine PEDOT:PSS, and Ti_3C_2-incorporated PEDOT:PSS materials

Film [a]	θ_{wat} (°)	θ_{oil} (°)	γ_d [b] (mN m^{-1})	γ_p [b] (mN m^{-1})	γ (mN m^{-1})	Solubility parameter δ (MPa$^{1/2}$)	Flory-Huggins interaction parameter χ
PTzBI-oF	61.9	91.2	24.63	0.03	24.66	18.21	/
PYF-T-o	46.4	86.1	26.12	0.29	26.41	18.85	/
PEDOT:PSS	42.0	68.6	38.59	1.14	39.73	23.12	χ_{13} = 6.20, χ_{23} = 4.67
Ti_3C_2:PEDOT:PSS	35.4	68.0	41.84	0.68	42.52	23.92	χ_{14} = 8.38, χ_{24} = 6.60

[a]To facilitate material identification in subsequent analyses, numerical labels were assigned as follows: 1 = PTzBI-oF (polymer donor), 2 = PYF-T-o (polymer acceptor), 3 = PEDOT:PSS (pristine AIL), and 4 = Ti_3C_2:PEDOT:PSS (Ti_3C_2-incorporated AIL); [b]The surface free energy components are denoted as γ_d and γ_p, representing the dispersion-force-induced and polar-force-induced contributions, respectively; PEDOT:PSS: poly(3,4-ethylenedioxythiophene):poly(styrenesulfonate); AILs: anode interfacial layers.

that Ti_3C_2 nanosheets can indeed lead to changes in the surface composition of PEDOT:PSS films.

In order to provide further evidence of the surface composition changes of PEDOT:PSS, the S elements on the surface of PEDOT:PSS and Ti_3C_2:PEDOT:PSS films were analyzed by XPS. As shown in Figure 6A, there are two types of peaks in the S 2p signal. The sulfur atoms in PSS correspond to bands ranging from

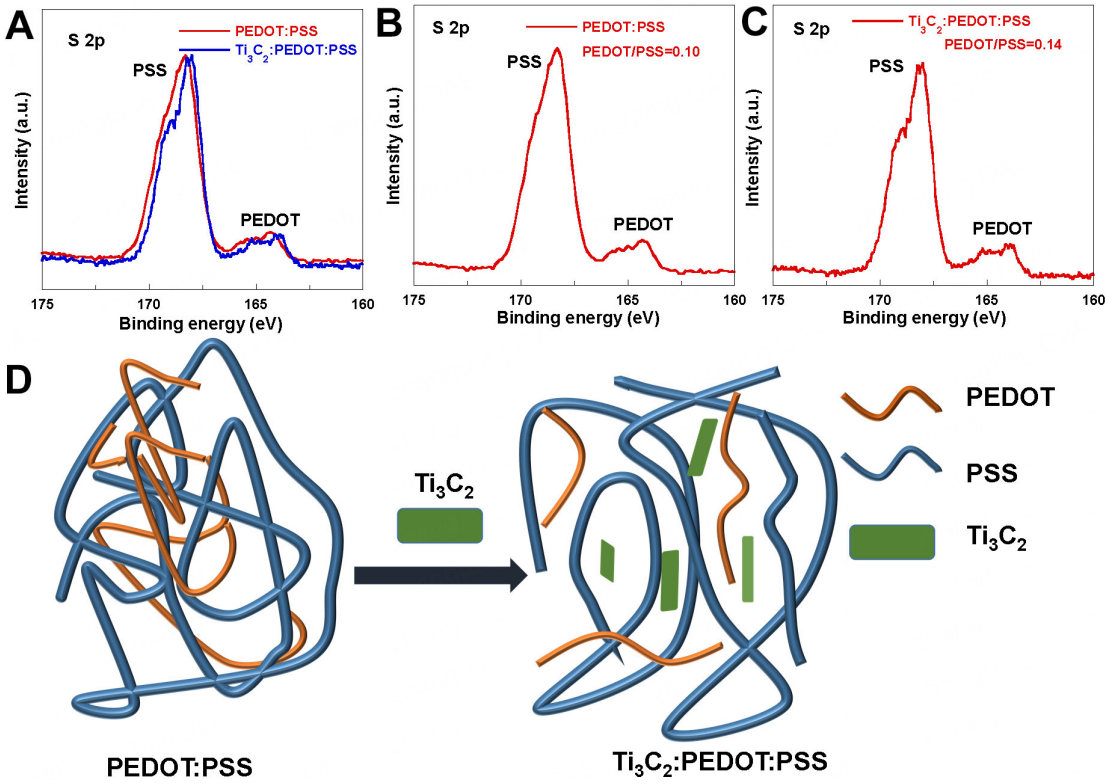

Figure 6. (A) XPS (S 2p) spectra for PEDOT:PSS and Ti_3C_2 :PEDOT:PSS films; (B) XPS (S 2p) spectra for PEDOT:PSS film; (C) XPS (S 2p) spectra for Ti_3C_2:PEDOT:PSS film; (D) Schematic illustration of the structural modification in the PEDOT:PSS film upon Ti_3C_2 doping. XPS: X-ray photoelectron spectroscopy; PEDOT:PSS: poly(3,4-ethylenedioxythiophene):poly(styrenesulfonate).

166-172 eV, while the sulfur atoms in PEDOT correspond to bands ranging from 162-166 eV. The S 2p peak at 164.5 eV can reflect the crystal configuration of PEDOT. It can be seen from Figure 6A that the S 2p peak moves from 164.5 eV to low-energy 163.7 eV, indicative of the enhanced crystal configuration of PEDOT, which induces part of the resonance structure in the PEDOT polymer chain changing from spiral benzoyl structure to linear quinone structure[60]. PEDOT molecular chains in spiral benzoyl state structure have stronger interchain interaction than spiral benzoyl state structure, which is conducive to the formation of PEDOT conductive nanocrystals with large grain size and tight packing, and larger conductive nanocrystals help to enhance the charge transfer between molecular chains. In addition, conductive Ti_3C_2 nanosheets connect discontinuous conductive nanocrystals to construct additional carrier transport channels[61]. Due to the highly conductive Ti_3C_2 nanosheets and interconnected conductive nanonetworks, the conductivity of the composite hole extraction layer greatly improved.

The peak area of PEDOT and PSS can be calculated by integration, and the relative components of PEDOT and PSS on the membrane surface can be represented by the ratio of PEDOT to PSS. The results showed that the PEDOT/PSS ratio of pure PEDOT:PSS films [Figure 6B] was 0.10. This is consistent with the common belief that the surface of PEDOT:PSS films contains more PSS. For Ti_3C_2:PEDOT:PSS films, the PEDOT/PSS ratio is estimated to be 0.14 [Figure 6C and Supplementary Table 7], which indicates that more conductive PEDOT components are enriched on the surface of the films after Ti_3C_2 doping into PEDOT:PSS. The increased conductivity of Ti_3C_2:PEDOT:PSS is well in accordance with the boosting trend of PEDOT/PSS ratio, which further confirms that the improved conductivity of Ti_3C_2:PEDOT:PSS is due to the redistribution of PEDOT and PSS chains. The chain rearrangement is mainly attributed to the fact that the Ti_3C_2 dopant is beneficial to the chain segment movement of PEDOT, which weakens the Coulomb force interaction between PEDOT and PSS.

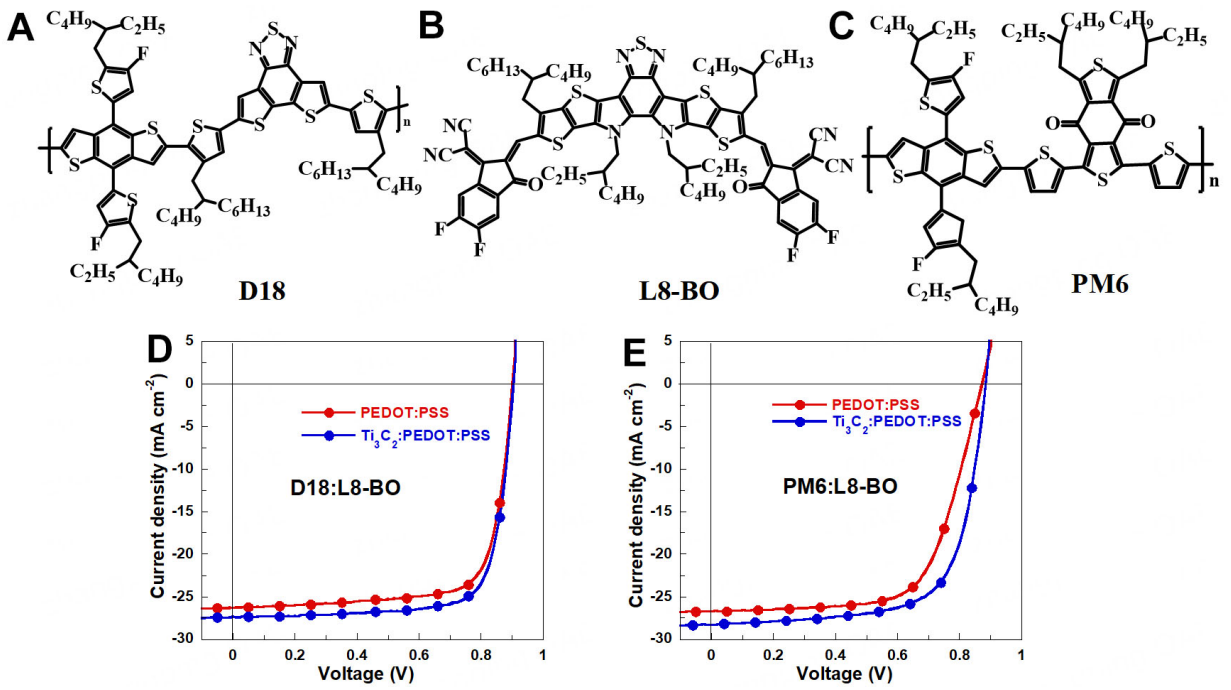

Figure 7. (A-C) Molecular structures of D18, L8-BO and PM6; *J-V* curves of (D) D18:L8-BO and (E) PM6:L8-BO devices with (or without) Ti_3C_2 in the PEDOT:PSS interlayer. PEDOT:PSS: Poly(3,4-ethylenedioxythiophene):poly(styrenesulfonate); *J-V*: current density-voltage.

Based on the above AFM, CA and XPS results, we propose the following mechanism: the size of PEDOT:PSS grains and PEDOT enrichment domains increase significantly after Ti3C2 doping. With the doping of Ti_3C_2, PEDOT changed from light bulb shape thin fiber to thick fiber, which represents the conformational change of PEDOT chain from spiral benzoyl structure with low electrical conductivity to linear quinone structure with strong electrical conductivity, and the nanophase separation of the film was enhanced [Figure 6D]. The grain size and crystallinity of PEDOT:PSS increase with the doping of Ti_3C_2, which is one of the main reasons for the high conductivity of Ti_3C_2:PEDOT:PSS.

The universal applicability of Ti_3C_2 doping strategy in PEDOT:PSS-based systems

To demonstrate the universal applicability of the Ti_3C_2 doping strategy in PEDOT:PSS-based systems, we fabricated OPV devices employing two distinct bulk heterojunction systems: D18:L8-BO and PM6:L8-BO, utilizing both pristine PEDOT:PSS and Ti_3C_2-doped PEDOT:PSS as AIL. Figure 7A-C displayed the molecular structures of D18, L8-BO and PM6, respectively. The *J-V* curves of D18:L8-BO and PM6:L8-BO devices with (or without) Ti_3C_2 in the PEDOT:PSS interlayer were measured under simulated AM 1.5G illumination [Figure 7D and E], with the homologous photovoltaic performance summarized in Supplementary Table 8. The incorporation of Ti_3C_2 into the PEDOT:PSS interlayer resulted in a significant enhancement of photovoltaic performance, with the D18:L8-BO-based device achieving a maximum PCE of 19.05%, a boosted J_{SC} of 27.37 mA cm^{-2}, and improved FF of 76.94%; the maximum PCE of the PM6:L8-BO device is increased to 17.33%, the J_{SC} is increased from 26.71 mA cm^{-2} to 28.31 mA cm^{-2}, and the FF is increased from 66.48% to 69.23%. The substantial enhancement in PCE observed in both D18:L8-BO and PM6:L8-BO-based OPVs conclusively demonstrates the universal applicability of the Ti_3C_2 doping strategy in PEDOT:PSS AIL. This innovative approach is anticipated to provide valuable guidance for the development of high-performance, universally applicable AIL in OPVs.

CONCLUSIONS

In summary, we prepared few-layer Ti_3C_2 nanosheets by HCl/LiF etching and doped them into PEDOT:PSS to fabricate OPV devices. As 2% volume of Ti_3C_2 doping into PEDOT:PSS interlayer, the maximum PCE of PTzBI-oF:PYF-T-o, D18:L8-BO, and PM6:L8-BO devices boosted from 15.61%, 17.92%, and 15.49% to 16.83%, 19.05%, and 17.33%, respectively. UPS results showed that Ti_3C_2 dopants regulated the energy level of PEDOT:PSS, and XPS analysis showed that Ti_3C_2 dopants induced the configuration change of PEDOT chain from spiral benzoyl structure with low electrical conductivity to linear quinone structure with strong electrical conductivity, and the nanophase separation of the film was enhanced. In addition, the highly conductive Ti_3C_2 nanosheet plays a connecting role in the PEDOT crystal, constructing a new charge transport channel, and thus realizing the improvement of hole extraction efficiency of PEDOT:PSS interlayer. The application of Ti_3C_2 doping PEDOT:PSS strategy is expected to bring new opportunities for boosting the intrinsic conductivity of PEDOT:PSS interlayer, so as to facilitate the fast hole extraction from the active layer to the anode and improve the PCE and stability of OPVs. Our work is expected to provide a novel two-dimensional crystal doping concept for efficient and universal AIL design toward high-performance OPVs.

DECLARATIONS

Author' contribution

Methodology and reviewing the original draft: Liu, Y. L.
Methodology, visualization, and reviewing the original draft: Wang, G.
Review and editing: Wang, W.; Guo, J.; She, L.; Liu, Z.
Methodology, conceptualization, supervision, funding acquisition, writing, review, and editing: Li, Z.
Funding acquisition, review, and editing: Wang, X.
Review, visualization and editing: Zheng, X.

Availability of data and materials

The data supporting the findings of this study are available within this Article and its Supplementary Materials. Further data are available from the corresponding authors upon request.

AI and AI-assisted tools statement

Not applicable.

Financial support and sponsorship

This work was financially supported by the National Natural Science Foundation of China (NSFC, Nos. 62404094 and 12305352), the Natural Science Foundation of Hunan Province (2023JJ40532), the National Key Research and Development Project funding from the Ministry of Science and Technology of China (No. 2021YFE0191500), the Natural Science Foundation of Hunan Province (2023JJ50132), Shenzhen Science and Technology Innovation Committee (Grants Nos. JCYJ20220818100211025, and KCXST20221021111616039), the Fund of University of South China (Nos. 210XQD018, 220XQD016), and the Fund of Hengyang Science and Technology Bureau (No. 202121014588).

Conflict of interest

All authors declared that there are no conflicts of interest.

Ethical approval and consent to participate

Not applicable.

Consent for publication

Not applicable.

Supplementary Materials

Supplementary Materials

REFERENCES

1. Li, Y.; Qi, F.; Fan, B.; et al. Eliminating the burn-in loss of efficiency in organic solar cells by applying dimer acceptors as supramolecular stabilizers. *Adv. Mater.* **2024**, *36*, 2313393. DOI
2. Cui, Y.; Chen, Z.; Zhu, P.; et al. Enhancing photostability and power conversion efficiency of organic solar cells by a "sunscreen" ternary strategy. *Sci. China. Chem.* **2023**, *66*, 1179-89. DOI
3. Yang, S.; Chen, Z.; Zhu, J.; et al. Guest acceptors with lower electrostatic potential in ternary organic solar cells for minimizing voltage losses. *Adv. Mater.* **2024**, *36*, 2401789. DOI
4. Zhang, C.; Zhong, X.; Sun, X.; et al. Designing a novel wide bandgap small molecule guest for enhanced stability and morphology mediation in ternary organic solar cells with over 19.3% efficiency. *Adv. Sci.* **2024**, *11*, 2401313. DOI PubMed PMC
5. Guo, C.; Sun, Y.; Wang, L.; et al. Light-induced quinone conformation of polymer donors toward 19.9% efficiency organic solar cells. *Energy. Environ. Sci.* **2024**, *17*, 2492-9. DOI
6. Fu, J.; Yang, Q.; Huang, P.; et al. Rational molecular and device design enables organic solar cells approaching 20% efficiency. *Nat. Commun.* **2024**, *15*, 1830. DOI PubMed PMC
7. Xu, R.; Jiang, Y.; Liu, F.; et al. High open-circuit voltage organic solar cells with 19.2% efficiency enabled by synergistic side-chain engineering. *Adv. Mater.* **2024**, *36*, 2312101. DOI
8. Zhang, G.; Chen, Q.; Zhang, Z.; et al. Co-La-based hole-transporting layers for binary organic solar cells with 18.82% efficiency. *Angew. Chem. Int. Ed.* **2023**, *62*, e202216304. DOI
9. Liu, Y.; Zhang, S.; Li, Y.; et al. Solution-processed molybdenum oxide hole transport layer stabilizes organic solar cells. *Chin. J. Polym. Sci.* **2023**, *41*, 202-11. DOI
10. Han, N.; Lee, M.; Moon, Y.; Yang, D.; Kim, D. Oxidized carbon materials as hole transport layers for high-performance organic photovoltaics. *Solar. RRL.* **2023**, *7*, 2200908. DOI
11. Yi, X.; Liu, H.; Li, Y.; et al. Solution-processed and thickness-insensitive hole transport layer for high efficiency organic solar cells. *J. Mater. Chem. C.* **2022**, *10*, 17521-9. DOI
12. Feaugas, F.; Nicolini, T.; Roche, G. H.; Hirsch, L.; Dautel, O. J.; Wantz, G. Homojunction doping for efficient hole extraction in polymer solar cells. *Solar. RRL.* **2023**, *7*, 2200815. DOI
13. Le, Q. V.; Nguyen, T. P.; Kim, S. Y. UV/ozone-treated WS_2 hole-extraction layer in organic photovoltaic cells. *Phys. Status. Solidi. RRL.* **2014**, *8*, 390-4. DOI
14. Yao, J.; Ding, S.; Zhang, R.; et al. Fluorinated perylene-diimides: cathode interlayers facilitating carrier collection for high-performance organic solar cells. *Adv. Mater.* **2022**, *34*, 2203690. DOI
15. Liu, L.; Chen, S.; Qu, Y.; et al. Nanographene-osmapentalyne complexes as a cathode interlayer in organic solar cells enhance efficiency over 18%. *Adv. Mater.* **2021**, *33*, 2101279. DOI
16. Xiong, X.; Xue, X.; Zhang, M.; et al. Melamine-doped cathode interlayer enables high-efficiency organic solar cells. *ACS. Energy. Lett.* **2021**, *6*, 3582-9. DOI
17. Li, J.; Qin, J.; Liu, X.; et al. Enhanced organic photovoltaic performance through promoting crystallinity of photoactive layer and conductivity of hole-transporting layer by V_2O_5 doped PEDOT:PSS hole-transporting layers. *Solar. Energy.* **2020**, *211*, 1102-9. DOI
18. Wang, Y.; Zhu, C.; Pfattner, R.; et al. A highly stretchable, transparent, and conductive polymer. *Sci. Adv.* **2017**, *3*, e1602076. DOI PubMed PMC
19. Kim J, Biswas S, Kim H. Evaluation of the impact of trivalent metal doping on the performance of titanium dioxide as an electron transport layer of Inverted-Structured organic solar cells. *Appl. Surface. Sci.* **2023**, *613*, 156052. DOI
20. Chen, Z.; Huang, Y.; Gao, J.; et al. Synchronous doping effects of cathode interlayers on efficient organic solar cells. *ACS. Energy. Lett.* **2022**, *7*, 4052-60. DOI
21. Liang, Q.; Han, J.; Song, C.; et al. Reducing the confinement of PBDB-T to ITIC to improve the crystallinity of PBDB-T/ITIC blends. *J. Mater. Chem. A.* **2018**, *6*, 15610-20. DOI
22. Kang, Q.; Liao, Q.; Yang, C.; Yang, Y.; Xu, B.; Hou, J. A new PEDOT derivative for efficient organic solar cell with a fill factor of 0.80. *Adv. Energy. Mater.* **2022**, *12*, 2103892. DOI
23. Randell, N. M.; Miclette, Lamarche. R.; Tintori, F.; Chernikov, R.; Welch, G. C.; Trudel, S. Photodeposited polyamorphous CuO_x hole-transport layers in organic photovoltaics. *ACS. Appl. Energy. Mater.* **2021**, *4*, 12900-8. DOI
24. Kim, T. G.; Ha, S. R.; Choi, H.; et al. Polymerizable supramolecular approach to highly conductive PEDOT:PSS patterns. *ACS. Appl. Mater. Interfaces.* **2017**, *9*, 19231-7. DOI

25. Zhao, B.; Huang, X.; Chung, S.; et al. Hole-selective-molecule doping improves the layer thickness tolerance of PEDOT:PSS for efficient organic solar cells. *eScience* **2025**, *5*, 100305. DOI
26. Rafique, S.; Roslan, N. A.; Abdullah, S. M.; et al. UV-ozone treated graphene oxide/ PEDOT:PSS bilayer as a novel hole transport layer in highly efficient and stable organic solar cells. *Org. Electron.* **2019**, *66*, 32-42. DOI
27. Moujoud, A.; Oh, S. H.; Shin, H. S.; Kim, H. J. On the mechanism of conductivity enhancement and work function control in PEDOT:PSS film through UV-light treatment. *Phys. Status. Solidi. (a).* **2010**, *207*, 1704-7. DOI
28. Huang, J.; Miller, P.; de, Mello. J.; de, Mello. A.; Bradley, D. Influence of thermal treatment on the conductivity and morphology of PEDOT/PSS films. *Synth. Met.* **2003**, *139*, 569-72. DOI
29. Li, Q.; Sun, Y.; Yang, C.; et al. Optimizing the component ratio of PEDOT:PSS by water rinse for high efficiency organic solar cells over 16.7%. *Sci. Bull.* **2020**, *65*, 747-52. DOI
30. Wei, Q.; Mukaida, M.; Naitoh, Y.; Ishida, T. Morphological change and mobility enhancement in PEDOT:PSS by adding co-solvents. *Adv. Mater.* **2013**, *25*, 2831-6. DOI PubMed
31. Cameron, J.; Skabara, P. J. The damaging effects of the acidity in PEDOT:PSS on semiconductor device performance and solutions based on non-acidic alternatives. *Mater. Horiz.* **2020**, *7*, 1759-72. DOI
32. Adedeji, M. A.; Hamed, M. S.; Mola, G. T. Light trapping using copper decorated nano-composite in the hole transport layer of organic solar cell. *Solar. Energy.* **2020**, *203*, 83-90. DOI
33. Lee, E. J.; Choi, M. H.; Han, Y. W.; Moon, D. K. Effect on electrode work function by changing molecular geometry of conjugated polymer electrolytes and application for hole-transporting layer of organic optoelectronic devices. *ACS. Appl. Mater. Interfaces.* **2017**, *9*, 44060-9. DOI PubMed
34. Liu, Y. L.; Zhang, C.; Guo, L.; et al. Synergistically adsorbing and reducing Uranium from water by a novel nano zero-valent copper/MXene 0D/2D nanocomposite. *Water. Res.* **2023**, *245*, 120666. DOI
35. Guo, L.; Liu, Y. L.; Zeng, Q.; et al. A self-driven solar coupling system with TiO_2@MXene cathode for effectively eliminating uranium and organics from complex wastewater accompanying with electricity generation. *J. Hazard. Mater.* **2024**, *465*, 133415. DOI
36. Bai, H.; Ma, R.; Su, W.; et al. Green-solvent processed blade-coating organic solar cells with an efficiency approaching 19% enabled by alkyl-tailored acceptors. *Nano-Micro. Lett.* **2023**, *15*, 241. DOI PubMed PMC
37. Li, T.; Wu, Q.; Yao, Z. F.; et al. Trialkylsilyl-thiophene-conjugated acceptor for efficient organic solar cells compatible with spin-coating and blade-coating technologies. *Sci. China. Chem.* **2024**, *67*, 4184-93. DOI
38. Gao, J.; Bai, H.; Li, P.; et al. Halogenated dibenzo[*f,h*]quinoxaline units constructed 2D-conjugated guest acceptors for 19% efficiency organic solar cells. *Adv. Sci.* **2024**, *11*, 2403334. DOI
39. Su, W.; Zhou, X.; Yao, Z. F.; et al. Halogenation strategy of thiophene derived solvent additives enables optimized morphology for organic solar cells with 19.17% efficiency. *Adv. Funct. Mater.* **2024**, *34*, 2313744. DOI
40. Lei, Y.; Shang, T.; Qiu, Y.; et al. Self-doped alcohol-soluble small molecules as cathode interface layers for organic solar cells. *Prog. Org. Coat.* **2025**, *200*, 109060. DOI
41. Wan, J.; Wen, R.; Xia, Y.; et al. All annealing-free solution-processed highly flexible organic solar cells. *J. Mater. Chem. A.* **2021**, *9*, 5425-33. DOI
42. Luo, D.; Jiang, Z.; Tan, W. L.; et al. Non-fused ring acceptors achieving over 15.6% efficiency organic solar cell by long exciton diffusion length of alloy-like phase and vertical phase separation induced by hole transport layer. *Adv. Energy. Mater.* **2023**, *13*, 2203402. DOI
43. Pei, S.; Xiong, X.; Zhong, W.; et al. Highly efficient organic solar cells enabled by the incorporation of a sulfonated graphene doped PEDOT:PSS interlayer. *ACS. Appl. Mater. Interfaces.* **2022**, *14*, 34814-21. DOI
44. Meng, H.; Liao, C.; Deng, M.; Xu, X.; Yu, L.; Peng, Q. 18.77 % efficiency organic solar cells promoted by aqueous solution processed cobalt(II) acetate hole transporting layer. *Angew. Chem. Int. Ed.* **2021**, *60*, 22554-61. DOI
45. Zhan, L.; Li, S.; Xia, X.; et al. Layer-by-layer processed ternary organic photovoltaics with efficiency over 18. *Adv. Mater.* **2021**, *33*, 2007231. DOI
46. Liu, Z.; Ma, X.; Xu, W.; et al. 15.28% efficiency of conventional layer-by-layer all-polymer solar cells superior to bulk heterojunction or inverted cells. *Chem. Eng. J.* **2022**, *450*, 138146. DOI
47. Li, Z.; Zhong, W.; Ying, L.; et al. Morphology optimization via molecular weight tuning of donor polymer enables all-polymer solar cells with simultaneously improved performance and stability. *Nano. Energy.* **2019**, *64*, 103931. DOI
48. Gasparini, N.; Salvador, M.; Fladischer, S.; et al. An alternative strategy to adjust the recombination mechanism of organic photovoltaics by implementing ternary compounds. *Adv. Energy. Mater.* **2015**, *5*, 1501527. DOI
49. Kyaw, A. K.; Wang, D. H.; Wynands, D.; et al. Improved light harvesting and improved efficiency by insertion of an optical spacer (ZnO) in solution-processed small-molecule solar cells. *Nano. Lett.* **2013**, *13*, 3796-801. DOI

50. Huang, Q.; Jing, J.; Zhang, K.; et al. Simultaneous improvement of efficiency and stability of inverted organic solar cell *via* composite hole transport layer. *J. Mater. Chem. A.* **2022**, *10*, 23973-81. DOI
51. Kim, M. S.; Jang, W.; Nguyen, T.; Wang, D. H. Morphology inversion of a non-fullerene acceptor via adhesion controlled decal-coating for efficient conversion and detection in organic electronics. *Adv. Funct. Mater.* **2021**, *31*, 2103705. DOI
52. Hamilton, R.; Shuttle, C. G.; O'Regan, B.; Hammant, T. C.; Nelson, J.; Durrant, J. R. Recombination in annealed and nonannealed polythiophene/fullerene solar cells: transient photovoltage studies versus numerical modeling. *J. Phys. Chem. Lett.* **2010**, *1*, 1432-6. DOI
53. Wood, S.; Blakesley, J. C.; Castro, F. A. Assessing the validity of transient photovoltage measurements and analysis for organic solar cells. *Phys. Rev. Applied.* **2018**, *10*, 024038. DOI
54. Deng, B.; Lian, H.; Xue, B.; et al. Niobium-carbide MXene modified hybrid hole transport layer enabling high-performance organic solar cells over 19. *Small* **2023**, *19*, 2207505. DOI
55. Wang, G.; Zhang, M.; Li, Z.; Wang, X.; Kang, X.; Ying, L. Efficient and stable organic solar cells enabled by incorporation of titanium dioxide doped PEDOT:PSS as hole transport layer. *Progress. in. Organic. Coatings.* **2023**, *183*, 107819. DOI
56. Shen, H.; Hu, T.; Huang, H.; Wu, D.; Xia, J. Promoting the photovoltaic performance and stability of organic solar cells by imidazole-doped PEDOT:PSS. *J. Mater. Sci:. Mater. Electron.* **2022**, *33*, 12083-92. DOI
57. Ding, X.; Ding, Y. F.; Huang, C.; et al. Non-covalent interaction enhancement on active/interfacial layers via two-dimensional vermiculite doping for efficient organic solar cells. *Small* **2024**, *20*, 2311715. DOI
58. Ye, L.; Collins, B. A.; Jiao, X.; Zhao, J.; Yan, H.; Ade, H. Miscibility-function relations in organic solar cells: significance of optimal miscibility in relation to percolation. *Adv. Energy. Mater.* **2018**, *8*, 1703058. DOI
59. Pang, S.; Zhang, R.; Duan, C.; et al. Alkyl chain length effects of polymer donors on the morphology and device performance of polymer solar cells with different acceptors. *Adv. Energy. Mater.* **2019**, *9*, 1901740. DOI
60. Modarresi, M.; Franco-Gonzalez, J. F.; Zozoulenko, I. Morphology and ion diffusion in PEDOT:Tos. A coarse grained molecular dynamics simulation. *Phys. Chem. Chem. Phys.* **2018**, *20*, 17188-98. DOI
61. Hou, C.; Yu, H. Modifying the nanostructures of PEDOT:PSS/$Ti_3C_2T_X$ composite hole transport layers for highly efficient polymer solar cells. *J. Mater. Chem. C.* **2020**, *8*, 4169-80. DOI